Balancing reservoir creation and seismic hazard in enhanced geothermal systems

V. Gischig,[1] S. Wiemer[1] and A. Alcolea[2,*]

[1]*Swiss Seismological Service, ETH Zürich, Switzerland. E-mail: gischig@sed.ethz.ch*
[2]*Geo-Energie Suisse AG, Zürich, Switzerland*

SUMMARY

Fracture shear-dilatancy is an essential process for enhancing the permeability of deep geothermal reservoirs, and is usually accompanied by the radiation of seismic waves. However, the hazard and risk perspective of induced seismicity research typically focuses only on the question of how to reduce the occurrence of induced earthquakes. Here we present a quantitative analysis of seismic hazard as a function of the two key factors defining an enhanced geothermal system: The permeability enhancement, and the size of the stimulated reservoir. Our model has two coupled components: (1) a pressure diffusion model and (2) a stochastic seismicity model. Permeability is increased in the source area of each induced earthquake depending on the amount of slip, which is determined by the magnitude. We show that the few largest earthquakes (i.e. 5–10 events with $M \geq 1.5$) contribute more than half of the total reservoir stimulation. The results further indicate that planning and controlling of reservoir engineering operations may be compromised by the considerable variability of maximum observed magnitude, reservoir size, the Gutenberg–Richter b-value and Shapiro's seismogenic index (i.e. a measure of seismic reactivity of a reservoir) that arises from the intrinsic stochastic nature of induced seismicity. We also find that injection volume has a large impact on both reservoir size and seismic hazard. Injection rate and injection scheme have a negligible effect. The impact of site-specific parameters on seismicity and reservoir properties is greater than that of the injected volume. In particular, conditions that lead to high b-values—possibly a low differential stress level—have a high impact on seismic hazard, but also reduce the efficiency of the stimulation in terms of permeability enhancement. Under such conditions, target reservoir permeability can still be achieved without reaching an unacceptable level of seismic hazard, if either the initial reservoir permeability is high or if several fractures are stimulated. The proposed methodology is a first step towards including induced seismic hazard analysis into the design of reservoir stimulation in a quantitative and robust manner.

Key words: Geomechanics; Permeability and porosity; Fracture and flow; Statistical seismology.

1 INTRODUCTION

Hydraulic stimulation of reservoirs has become a standard technique for increasing the permeability of enhanced geothermal systems (EGS; Häring *et al.* 2008; Petty *et al.* 2013), hydrothermal systems (Majer *et al.* 2007) and oil and gas reservoirs (de Pater & Baisch 2011). During stimulation, fluid is injected into the rock mass at high pressure. The reduction in effective normal stress induces (i) slip along pre-existing fractures if frictional resistance is overcome (i.e. hydroshearing), and/or (ii) fracture opening if tensional strength is exceeded (i.e. hydrofracturing; Cladouhos *et al.*

2013). For enhancing permeability hydroshearing tends to be more efficient, because shear-dilation associated with slip increases fracture aperture in an almost irreversible manner due to dislocation of asperities on the fracture walls. Hydroshearing is usually accompanied by micro-earthquakes because dynamic slip along fractures radiates seismic energy. Hence, induced seismicity is an essential ingredient for permeability enhancement, but the associated nuisance and potential seismic hazard and risk is a serious threat for EGS projects. A number of past projects involving fluid injection into a reservoir have been affected by the negative impact of seismicity (e.g. waste water injection (Ellsworth 2013; Keranen *et al.* 2013) or EGS projects Häring *et al.* (2008)). During EGS stimulation, most of the events are micro earthquakes of magnitude <2.5 that are usually not felt. However, because the size of induced

*Now at: TK Consult AG, Zürich, Switzerland.

earthquakes cannot be readily controlled nor limited, larger earthquakes cannot be excluded, and may be felt by the population or even cause damage. For instance, in the city of Basel (Switzerland), two felt events caused strong opposition by the local population. The subsequent risk study concluded that the creation and operation of an EGS with the planned stimulation regime within the Basel underground and given the high population density would be too costly (Baisch *et al.* 2009), a finding which ultimately led to the suspension of the project (Giardini 2009). Thus, induced seismicity poses a serious hazard that needs to be coped with, not only because of nuisance to the population, but also because a large magnitude event causing structural damages cannot be fully excluded (Majer *et al.* 2012).

Ways to limit induced seismicity to a useful but not harmful level are currently being explored by a wide scientific community. Main research lines range from analysing case studies to the use of computational methods based on numerical reservoir models. Case studies are collected to find a possible link between site characteristics (e.g. tectonic regime, tectonic seismic hazard, rock type) or injection characteristics (e.g. injection pressure, volume, reservoir depth) and induced seismic hazard (Evans *et al.* 2012). Currently, such studies provide no conclusive recommendations on how to limit induced seismicity by a safe choice of the project site. Such empirical studies demonstrate that the factors defining the level of induced seismicity are numerous (e.g. tectonic setting, rock type, depth, injection volume, etc.), and that the number of accessible case studies with good data quality is severely limited (Evans *et al.* 2012).

Most research addressing seismic hazard in EGS projects focuses on finding ways to reduce induced seismicity. Such studies do not consider the question, if a reservoir created or enhanced at an acceptable level of seismicity has become sufficiently large and permeable for commercially viable heat extraction. In reservoir stimulations with considerable seismicity (even including felt events), permeability was locally increased by a factor >100 (e.g. about 200–400 times in Basel, Häring *et al.* (2008); about 200 times in Soultz-sous-Forêts; Evans 2005). In contrast, there are cases where seismicity was very limited but so was permeability enhancement. In Ogachi, Japan, reported magnitudes were mostly below *M*-1.0 (except for a single *M*2.0; Kaieda *et al.* 2005). However, permeability increased only by a factor of about 20 and fluid recovery rate stayed at a low level of about 25 per cent (Kaieda *et al.* 2005).

We present a suite of numerical injection experiments that give insights into the relationship between induced seismic hazard analysis (ISHA) and reservoir creation by hydroshearing. For this, we couple the stochastic seismicity model described by Goertz-Allmann & Wiemer (2013) and Gischig & Wiemer (2013) to a fluid flow model. Unlike those studies, in our model permeability increases as a consequence of seismic events, hence ensuring coupling between seismicity and flow field in both directions. Note that we only focus on hydroshearing as reservoir stimulation mechanism that enhances permeability mostly irreversibly. We do not consider hydrofracturing, which predominantly produces reversible permeability changes. The basic assumption in our approach is that the entire permeability enhancement is produced by seismic slip, whereas the contribution of potential aseismic slip is ignored. Through the ability to compute a large number of stochastic seismicity catalogues, and the corresponding distributions of permeability enhancement, we can address the questions:

(1) What event magnitudes are most efficient in enhancing permeability?

(2) How predictable are seismic hazard and target reservoir size, given the uncertainties in our knowledge of stress distribution and fault locations, and the inherent randomness of the processes controlling stimulation?

(3) What level of induced seismic hazard should be anticipated for a certain target size of the enhanced reservoir?

(4) What conditions lead to successful permeability enhancement without exceeding predefined hazard seismic levels?

2 METHOD

Our modelling approach consists of two components: (1) a fluid flow model that computes transient pressure disturbances and (2) a stochastic seismicity model that uses the transient pressure field as input to induce earthquakes at potential earthquake hypocenters (i.e. the so-called seed points). Our study is limited to 2-D. Thus, the model represents an equivalent continuum of a medium containing a single large fracture plane that accommodates all flow and slip, and that is optimally oriented in the ambient stress field. As we assume a strike-slip stress regime for all our models, the model represents a subvertical fracture that is penetrated by a subhorizontal borehole. The open-source code SUTRA is used as flow simulator (Voss & Provost 2010). The stochastic seismicity model is presented by Goertz-Allmann & Wiemer (2013) and Gischig & Wiemer (2013). These two basic components are explained in detail below.

2.1 The fluid flow model

SUTRA (Saturated-Unsaturated TRAnsport; Voss & Provost 2010) is a finite element code that solves the fluid flow as well as the solute or energy transport equations. For the purpose of this study, we simplified the code to only solve for pressure diffusion (i.e. fluid mass balance) in a saturated porous medium. The governing equation is:

$$\rho S_{op} \frac{\partial p}{\partial t} = \nabla \cdot \left(\frac{\rho \underline{\underline{k}}}{\mu} \nabla p \right) + Q_p, \tag{1}$$

where ρ (kg m^{-3}) is fluid density, μ (Pa · s) dynamic viscosity, S_{op} (Pa^{-1}) is specific pressure storativity, $\underline{\underline{k}}$ (m^2) the intrinsic permeability tensor, p (Pa) is pressure and Q_p [kg (m^3 · s)$^{-1}$] the mass source of fluid per unit volume of the medium.

The 2-D model presented here represents a single fracture surface or a fracture zone contained within the 2-D modelling domain. Since our model is an equivalent continuum representation of a fractured medium, it assumes that fracture connectivity is between sufficiently high to allow hydraulic communication in the entire 2-D domain. Although the fracture is assumed to be subvertical, gravity is not considered in our model. We further neglect depth dependent permeability that may arise from increasing mean stresses with depth (Ingebritsen & Manning 2010). Gravity and depth-dependent permeability result in two opposite effects that may balance each other to some unknown degree. Hence, we ignore both effects for simplicity. The model domain is discretized with a regular mesh with square elements with side lengths of 15 m. The fluid is injected at the centre of the domain. We use time steps of 100 s to model the pressure field, which is passed on to the stochastic seed model every 1000 s.

2.2 The stochastic seismicity model

The stochastic seismicity model uses the pressure field computed by SUTRA to decide if events have been induced. The model was
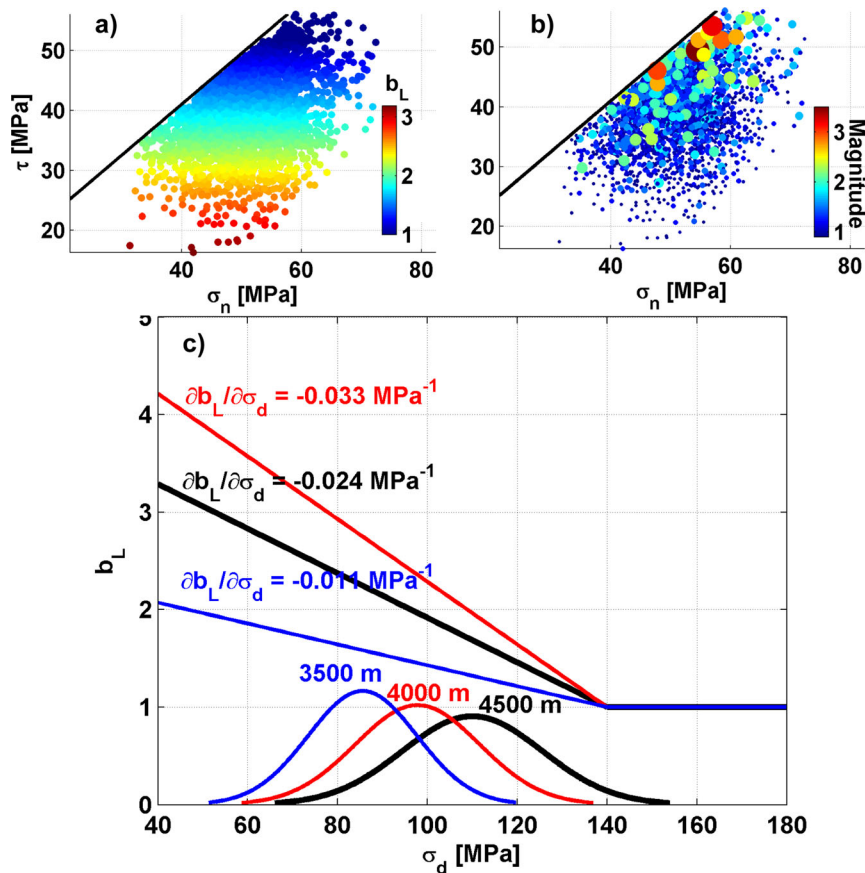
Figure 1. (a) Seed points shown in a Mohr Coulomb diagram (effective normal stress versus shear stress diagram). The seed points are assigned a local b-value b_L depending on the differential stress σ_d using the relationship in (c) (black line). The differential stresses are computed using mean values of $\sigma_3 - p_f = 30$ MPa and $\sigma_1 - p_f = 140$ MPa and a 10 per cent standard deviation around the mean [see also black probability distribution function in (c)]. Optimal orientation of the stress field is assumed for all seed points. (b) For each seed point in (a) a random magnitude is drawn from a Gutenberg–Richter distribution with b-value b_L. (c) $b_L - \sigma_d$ relationships and probability distribution functions of σ_d used in this study. Black lines represent the parameters used for the reference model (Figs 2 and 3) and correspond to the values found by Gischig & Wiemer (2013) to best-fit observed seismicity in Basel. Blue and red lines correspond to the alternative scenarios used in Figs 5–7.

described by Goertz-Allmann & Wiemer (2013) and Gischig & Wiemer (2013) and is based on the approach suggested by Rothert & Shapiro (2003). We outline here the basic steps of the stochastic seismicity model:

(1) *Initiation of the seed field:* Seed points (i.e. potential hypocentre locations) are randomly distributed over the 2-D domain. They are attributed with two principal effective stress components σ_1 and σ_3, representative of the regional stress field. *In situ* pore-pressure is assumed to be hydrostatic prior to stimulation. The stress components are sampled from normal distributions with mean values corresponding to the ambient stress field, and a standard deviation of 10 per cent of the mean (Fig. 1). Hence, the seed points are all assigned a normally distributed differential stress σ_d. Based on a Mohr–Coulomb failure criterion (described by a friction angle φ and cohesion c), and an assumed orientation in the stress field (here optimal orientation is used throughout), we compute for each seed point the pressure that is required for failure to occur. At initiation of the seed point population the stress state at those seed points that are above the Mohr–Coulomb failure criterion (i.e. those that already above the failure limit without pressurization, and thus represent unstable stress states) are redrawn. This is repeated until a population of stable seed

points is obtained, that is until all seed points have a stress state that is stable according to the Mohr–Coulomb failure criterion (Fig. 1a).

(2) *Inducing seismic events:* When the overpressure at a seed point (which is updated after each time step) exceeds the previously calculated failure pressure, the seed point slips. The following strategy suggested by Goertz-Allmann & Wiemer (2013) is then used to assign an event magnitude. Assuming a negative linear relationship between local differential stress σ_d and b-value (i.e. $\partial b_L / \partial \sigma_d < 0$), each seed point is also assigned a local b-value b_L (Fig. 1c). The assumption is inspired by observations of natural seismicity (e.g. Schorlemmer *et al.* 2005; Spada *et al.* 2013) and acoustic emissions in laboratory tests (e.g. Amitrano 2012). A random magnitude is then drawn from a distribution of 10^5 magnitudes represented by the seed point local b-value. To illustrate this process, the seed points in Fig. 1(a) are assigned a random magnitude in Fig. 1(b). The random local b-value b_L (i.e. obtained from a random differential stress), as well as the random drawing of event magnitudes are the key stochastic elements of this approach. We stress here that the local b-value b_L is not be confused with the b-value of a modelled or observed sequence of induced seismic events. It is merely part of the stochastic procedure that allows random drawing of magnitudes with resulting spatial and temporal variability of b-values of a sequence of events
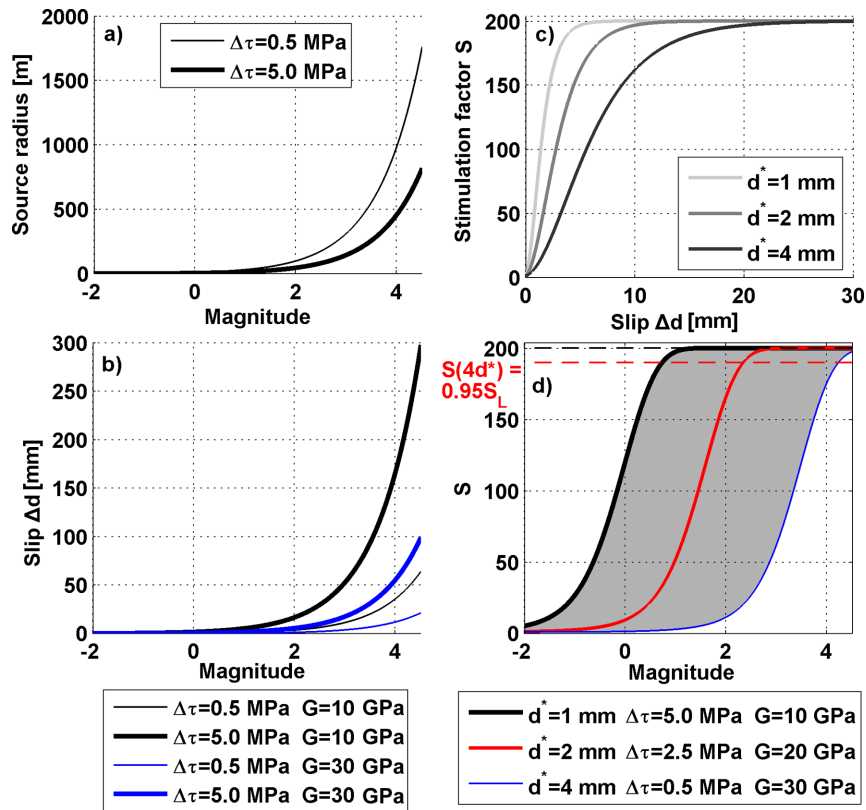
Figure 2. (a) Scaling laws (eqs 2 and 3) relating magnitude to earthquake source radius. (b) eqs (2) and (5) relating magnitude to earthquake source area and slip. (c) Relationship between slip and permeability enhancement according to eq. (6) using a maximum stimulation factor $S_L = 200$. (d) Relationship between magnitude and stimulation factor illustrating the parameterization in this study. We show two 'extreme' curves using the parameters in (a)–(c) that produce the largest (black) and the smallest permeability enhancement (blue). The red curve is the intermediate case corresponding to the parameters used in this study (Table 1). The magnitudes that result in 95 per cent of the maximum stimulation efficiency are 0.7, 2.3 and 4.2 for the three cases.

as observed by Bachmann *et al.* (2012) for Basel. Fig. 1(c) displays distributions of differential stress at different reservoir depths and the relationships between b_L and σ_d used in this study. The black lines correspond to the parameters that best fit the seismicity data observed in the Basel EGS project (Gischig & Wiemer 2013), and are the ones used for the reference example in Section 3.1.

(3) *Compute source properties and a new stress state:* The relationship by Hanks & Kanamori (1979) is used to convert magnitude into moment M_0:

$$M_0 = 10^{1.5(M_w+6.03)}. \tag{2}$$

Source dimensions of the induced events are obtained by using the relationship by Eshelby (1957), assuming a circular shape of the source area:

$$M_0 = \frac{17}{6}\Delta\tau \cdot r^3, \tag{3}$$

where $\Delta\tau$ is stress drop (Pa) and r (m) is the radius of the circular source area. Eqs (2) and (3) are illustrated in Fig. 2(a). Stress drop is assumed to be proportional to initial effective normal stress (i.e. before pressurization due to injection at time $t = 0$):

$$\Delta\tau = \mu_{\Delta\tau}\sigma_{n,eff}(t = 0). \tag{4}$$

The assumption is based on the notion that at onset of slip the friction—and thus shear stress—drops from a peak friction angle to a residual friction angle (e.g. Garagash & Germanovich 2012), with the difference corresponding to $\mu_{\Delta\tau}$. A value of $\mu_{\Delta\tau} = 0.05$ means that the stress drop $\Delta\tau = 2.5$ MPa at an initial effective

normal stress of 50 MPa, which is in agreement with reported stress drop values from the EGS in Basel (Goertz-Allmann *et al.* 2011). We subtract this stress drop value from the current shear stress of the failed seed point to get a new shear stress. Thus, the seed point obtains a stable stress state again and can be retriggered if pressurized to a higher level. Note that shear stress is recomputed not only for the seed points that fail, but also for all those that are within the radius r from the triggered seed point, that is all seed points within the source area of the triggered seed point undergo the same stress change.

2.3 Coupling of seismicity and permeability

Each induced seismic event is used to modify the permeability field for the subsequent time steps of the transient pressure model. The average slip Δd on the source area A of a seismic event can be computed from

$$M_0 = GA\Delta d = Gr^2\pi\Delta d, \tag{5}$$

where G (Pa) is the elastic shear modulus of the medium (Fig. 2b) and r is the radius of the source area according to eq. (3). Slip on fractures is associated with shear dilation, that is, the hydraulic aperture increases and thus permeability is enhanced. The increase of permeability can reach two to three orders of magnitudes as reported by several authors (e.g. Esaki *et al.* 1999; Lee & Cho 2002; Evans 2005; Häring *et al.* 2008; Mitchell & Faulkner 2008). To compute permeability increase from slip, we follow observations by Lee & Cho (2002) and Esaki *et al.* (1999). They present

Table 1. Model input parameters.

Parameter	Value
Stress regime	Strike-slip
Depth	4500 m
σ_1	185 MPa
σ_3	75 MPa
Hydrostat. pressure	45 MPa
Seed number	20 000 (1 point per 8×8 m)
b_L	$\partial b_L / \partial \sigma_d = 0.024$ MPa^{-1}, $\sigma_d < 140$ MPa, and $b_L = 1.0$, $\sigma_d > 140$ MPa
$\mu_{\Delta\tau}$	0.05
G	20 GPa
k_0	4e–17 m^2
S_p	1e–11 Pa^{-1}
S_L	200
d^*	2 mm

laboratory observations of permeability change dependent on slip, and find permeability increases by two to three orders of magnitude, but only up to a certain amount of slip. For shear displacements greater than about 10 mm, permeability stayed at a constant level. These studies showed that the shear displacement at which permeability does not increase anymore is larger at higher normal stresses. We propose a function of permeability k that accounts for the fact that permeability increases only up to a certain limiting factor S_L (Fig. 2c). The equivalent porous medium permeability k of a medium that consists of a single fracture contained in low-permeability rock is $k = T_f/h$ (i.e. we assume that the rock permeability k_r (m^2) is several orders of magnitude smaller than the fracture permeability $k_f \gg k_r$). Here, T_f [m^3] is the fracture transmissibility and h (m) is the thickness of the layer being modelled. The latter corresponds to the off-plane thickness of our 2-D model, which corresponds to a slice of a translation symmetric 3-D model. In our case, it corresponds to an openhole section of $h = 100$ m. We suggest the following relationship to compute relative permeability change as a function of slip Δd:

$$\frac{k}{k_0} = \frac{T_f}{T_{f0}} = \left[1 + C\left(1 - e^{-\frac{\Delta d}{d^*}}\right)\right]^n. \tag{6}$$

Note that, if $\Delta d \gg d^*$, permeability k will tend to the maximum possible value that is S_L times the initial value k_0: $k(\Delta d \rightarrow \infty) = k_0 S_L = k_0 (1 + C)^n$. Thus, d^* determines the amount of slip required to reach close to the maximum possible permeability increase. The limiting factor S_L for permeability at large amounts of slip Δd is related to the constant C as $C = \sqrt[n]{S_L} - 1$. A comparison to laboratory shear experiments by Lee & Cho (2002) and Esaki *et al.* (1999) showed that slip versus permeability data can be fit reasonably well with $n = 3$, and d^* in the range of 2–3 mm. Their experiments covered only a normal stress range of 1–20 MPa, whereas normal stresses on optimally oriented fractures at 4500 m depth are in the range of about 40–70 MPa (based on parameters in Table 1). Since a systematic evolution of d^* with normal stress could not be observed in those laboratory experiments, we use $d^* = 2$ mm in our study unless explicitly stated. Further, S_L is set to 200 in all our models following the observations in Basel (Häring *et al.* 2008). Note that at a slip of $\Delta d = 4d^*$, 95 per cent of S_L is reached.

Fig. 2(d) shows the permeability increase in relation to magnitude. To illustrate a range of possible permeability enhancement curves, we show two 'extreme' cases: For a stress drop of $\Delta\tau = 5.0$ MPa and a shear modulus $G = 10$ GPa, slip created by an earthquake of a certain magnitude is more than one order of magnitude larger than for $\Delta\tau = 0.5$ MPa and $G = 30$ GPa and the same event magnitude. Combined with values of $d^* = 1$ and 4 mm, 95 per cent of the maximum permeability enhancement S occurs at magnitudes $M0.7$ or $M4.2$, respectively. In our study, we use an intermediate case with $\Delta\tau \approx 2.5$ MPa, $G = 20$ GPa and $d^* = 2$ mm, for which 95 per cent of S_L occurs for magnitudes $M2.3$ (red curve in Fig. 2d).

Although we acknowledge that permeability changes may also have a reversible, pressure-dependent component, we only focus on irreversible permeability changes for simplicity. Further, we do not consider changes of storativity, as quantitative observations on slip-induced storativity changes do not exist to our knowledge. Hence, the assumption is in agreement with the model strategy used by Miller *et al.* (2004), McClure & Horne (2011) and Cappa *et al.* (2009).

2.4 Size of the stimulated reservoir

The size of the stimulated reservoir is usually derived from the extent of the seismic cloud. We express the size of the reservoir by a circle with radius R_{seis} that contains 95 per cent of all the seismic events. Note that this value is not informative on how strongly the medium within this radius was stimulated. If only a few small seismic events occur within this radius, the average permeability within the reservoir is not strongly enhanced. In contrast, large events and a high event density create a much stronger permeability enhancement. We introduce the parameter SE—here termed 'stimulation efficiency'—that describes the ratio of the average (or effective) stimulation in the reservoir to the maximum possible stimulation S_L. The integration of the stimulation factor $S(x,y) = k(x,y)/k_0$ over the entire model domain with total area A, yields a total stimulation factor S_{total}:

$$S_{total} = \int_A [S(x, y) - 1]\partial A. \tag{7}$$

The subtraction of 1 is done to exclude from integration areas that were not stimulated at all. If the medium within the radius R_{seis} would be stimulated uniformly by an average, effective stimulation factor S_{eff}, the total stimulation value of a circular shaped uniform reservoir becomes

$$S_{total}^{uniform} = (S_{eff} - 1) \cdot \pi R_{seis}^2. \tag{8}$$

Setting eqs (10) and (11) equal allows us to compute an effective stimulation factor S_{eff} that indicates how strongly the reservoir was stimulated by comparing it to an equivalent circular and uniformly stimulated reservoir with radius R_{seis}.

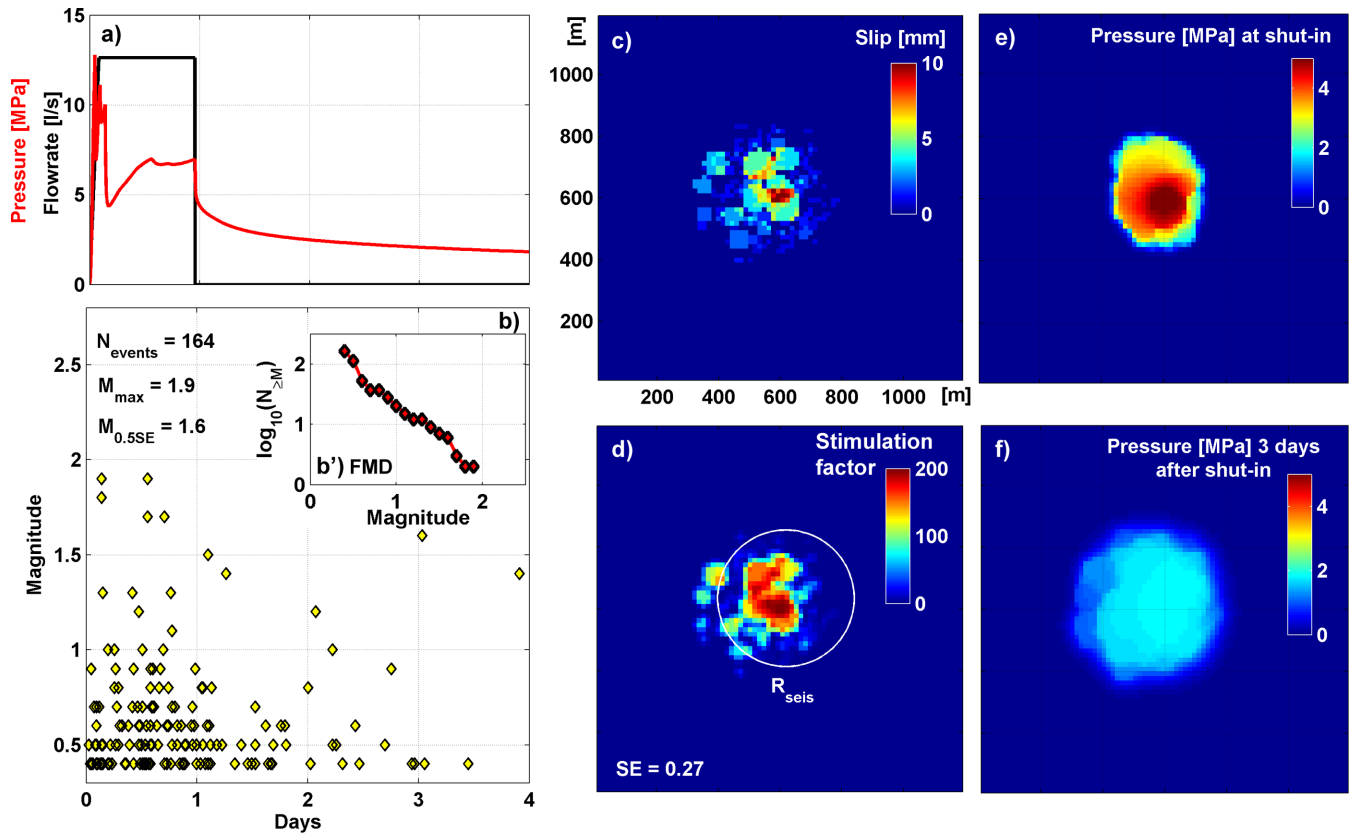$$(S_{eff} - 1) = \frac{\int_A [S(x, y) - 1]\partial A}{\pi R_{seis}^2}. \tag{9}$$

We can then define the stimulation efficiency as:

$$SE := \frac{(S_{eff} - 1)}{(S_L - 1)}. \tag{10}$$

3 RESULTS

3.1 Reference case

In Figs 3(a)–(d), the result of one representative stochastic model realization is shown, for which the parameters in Table 1 are used. The parameters of the stochastic seed model are those obtained by

Figure 3. Injection flow rate and modelled injection overpressure for a single stochastic realization. (b) Seismic event magnitudes. The inset (b') shows the frequency–magnitude distribution (FMD) of the seismic event sequence. (c) Slip field computed from the seismic events shown in (b) and (d) using eqs (2)–(5). (d) Stimulation factor computed from the slip field in (c) and eq. (6). (e) Pressure field at shut-in after about one day of injection. (f) Pressure field at the end of the stimulation experiment.

Gischig & Wiemer (2013) in an attempt to reproduce the seismicity data of the stimulation in Basel. As hydraulic parameters, we chose reasonable values for an equivalent porous medium of crystalline rock containing a single fracture that takes all flow (e.g. Häring *et al.* 2008), and an open borehole section of $h = 100$ m (Table 1). A flow rate of 12.5 l s^{-1} is injected for one day (Fig. 3a), which gives a total injection of 1080 m^3. Three more days were simulated to minimally capture the post-injection seismicity. The resulting injection pressure reaches maximum values of up to 13 MPa, and exhibits some strong pressure drops. These pressure drops occur as a consequence of strong permeability enhancement due to the largest events. In total 164 events larger than the magnitude of completeness of $M_c = 0.4$ occur (Fig. 3b). The *b*-value of the entire sequence is 1.41. The accumulated slip is shown in Fig. 3(c), and the resulting permeability enhancement in Fig. 3(d). The reservoir size, as measured by the equivalent radius R_{seis} derived from the seismic cloud (i.e. the observable reservoir size), is the circle in Fig. 3(d). The pressure fields at shut-in and at the end of the modelled period are shown in Figs 3(e) and (f). The stimulation efficiency SE is 0.27, which implies that the reservoir was stimulated on the average by a factor $S_{eff} = 55$. We also compute how much each event contributes to the final stimulation efficiency in terms of percentage of SE. The magnitude that defines the threshold, above or below which the events contribute 50 per cent to the stimulation efficiency is here termed $M_{0.5SE}$. For the single realization shown in Fig. 3 it is $M_{0.5SE} = 1.6$. It implies that the six events with magnitudes between 1.6 and 1.9 contribute half of the reservoir stimulation, whereas the remaining 158 events contribute the other half.

The results of 500 model realizations are summarized in Fig. 4. The median of the number of induced magnitudes greater than $M_c = 0.4$ is 167 (95 percentile range 105–199). Fig. 4(a) shows the considerable variability of R_{seis} (245 m on average). Similarly, SE strongly varies around a mean value of 0.24. Extreme SE values are even greater than 1, which means that a number of events occurred with source radii larger than the one defined only by event hypocenters. These events stimulated the entire source area by nearly the maximum possible value $S_L = 200$. They correspond to events, for which the source area has run out the stimulated area. Fig. 4(c) shows the *b*-values of all realizations (1.43 on average). Although always the same parameter sets were used, the stochastic process of randomly drawing magnitudes from a Gutenberg–Richter distribution with variable local *b*-values (Gischig & Wiemer 2013) produces a considerable variability of the final *b*-value of the entire sequence. Fig. 4(d) shows the variability of the seismogenic index Σ (-0.37 on average). The seismogenic index was first introduced by Shapiro *et al.* (2010) and describes the readiness of rock mass to react to injection by releasing seismic energy:

$$\log_{10}(N_{M \geq M_i}) = \Sigma + \log_{10}[Q(t)] - bM_i, \tag{11}$$

where $Q(t)$ [m^3] is the injected volume up to a time t. Comparing eq. (11) with the Gutenberg–Richter law $\log_{10}(N_{M \geq M_i}) = a - bM_i$ reveals that the seismogenic index represents the Gutenberg–Richter *a*-value normalized by the injected volume (i.e. it is by definition independent of injection volume). Since the seismogenic index is only defined during fluid injection (i.e. not after shut-in; Shapiro *et al.* 2010), we computed Σ only for events before shut-in (Fig. 4d). The
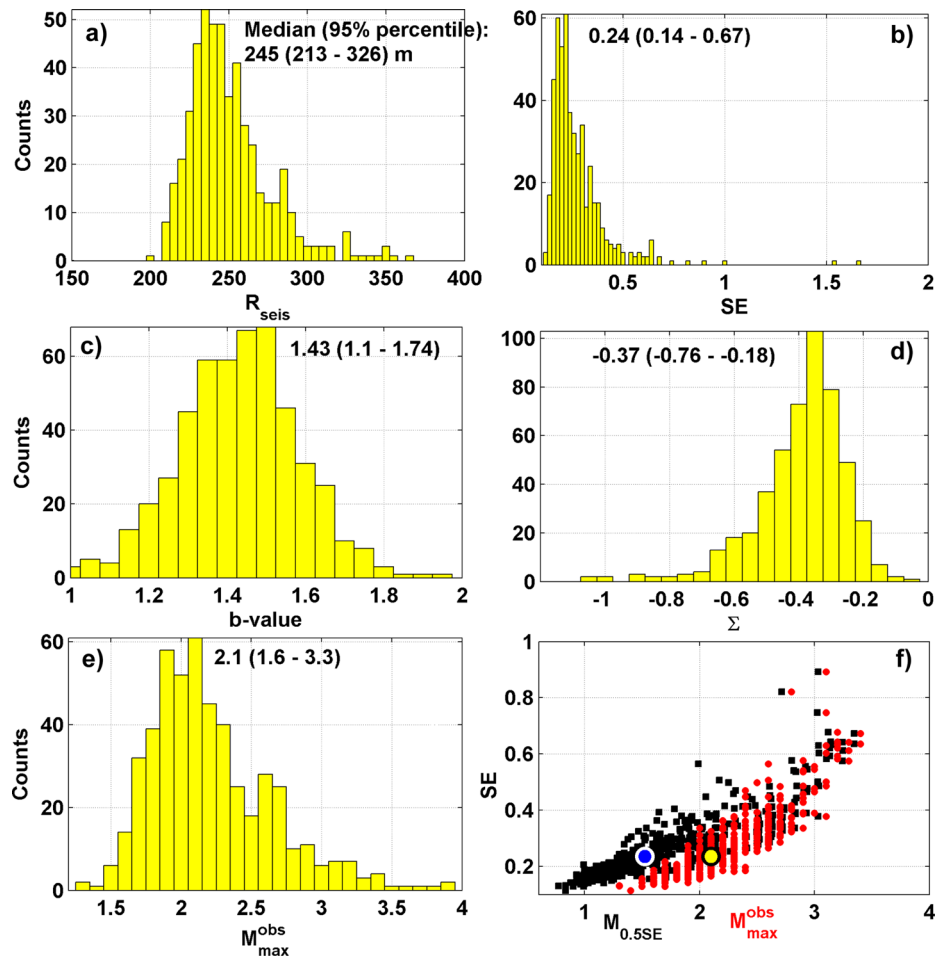
Figure 4. Histograms summarizing the result of 500 realizations of the stochastic model. (a) Reservoir radii R_{seis}. (b) Stimulation efficiency SE. Also indicated are median value and 95 percentiles. (c) b-values. (d) Seismogenic index Σ. (e) Maximum observed magnitude of each realization. (f) Relationship between stimulation efficiency and maximum observed magnitude and the magnitude $M_{0.5SE}$, above and below which 50 per cent is contributed to stimulation efficiency. The correlation indicates that large magnitudes are most relevant for the final reservoir stimulation.

maximum observed magnitude in each realization $M_{max(obs)}$ is presented in Fig. 4(e). While the mean value is 2.1 [expectation value of maximum magnitude $M_{max(exp)}$] also magnitudes between 1.6 and 3.3 are expected based on a 95 per cent confidence interval. Fig. 4(f) shows SE versus $M_{max(obs)}$ and $M_{0.5SE}$. Despite significant scatter certain correlation is observable. Higher stimulation efficiency occurs both for larger maximum magnitudes and larger $M_{0.5SE}$. The role of the largest events in enhancing permeability is further explored in Section 3.3.

3.2 Sensitivity to injection strategy and site-specific conditions

We investigated the impact of different injection scenarios on the model results (Fig. 5). In a first suite of models, we explore the role of injection volume. The injection rate in Fig. 4(a) was used, but the duration of the injection period was changed such that 540, 1080, 1620 or 2160 m³ are injected in total (note that 1080 m³ is the reference case). The results for R_{seis}, SE, $M_{max(obs)}$, b-value and Σ are presented as cumulative density functions (CDF). Increasing the total injection volume has an impact on R_{seis}, SE and $M_{max(obs)}$. The relationship between injection volume and hazard [expressed as in terms of $M_{max(obs)}$] was already shown by

Gischig & Wiemer (2013). Larger injection volumes stimulate not only larger areas, but also in a more efficient manner because the probability of larger events increases with volume, and larger events have the strongest impact on permeability enhancement. The median of the b-value does not change, but its variability decreases for larger volumes, because more events are induced, which results in a more stable estimate of the b-value. The seismogenic index Σ does not vary for different volumes. This is in agreement with the assumption by Shapiro *et al.* (2010), who argue that the seismogenic index is a site-specific parameter and therefore does not depend on volume.

In a second suite of models, the role of the injection pressure (or rate) is investigated, while keeping the total volume constant (Fig. 5b). Injection rate (and hence pressure) has a very small impact on model results. R_{seis} and $M_{max(obs)}$ do not change. A small effect can be observed for the ratio SE, which shifts from 0.47 to 0.50 for the lowest and the highest injection rate, respectively. Note that the mean number of events also increases from 140 to 180 on average. Thus, injecting at higher rates is slightly more efficient in enhancing permeability. The effect is small because at higher rates it is mostly the number of small events that increases. A small impact can also be observed on both b-value and Σ. The median of the b-value increases from 1.38 to 1.43, and the median of Σ from −0.41 to −0.35 from the lowest to the highest injection rate. Thus, we
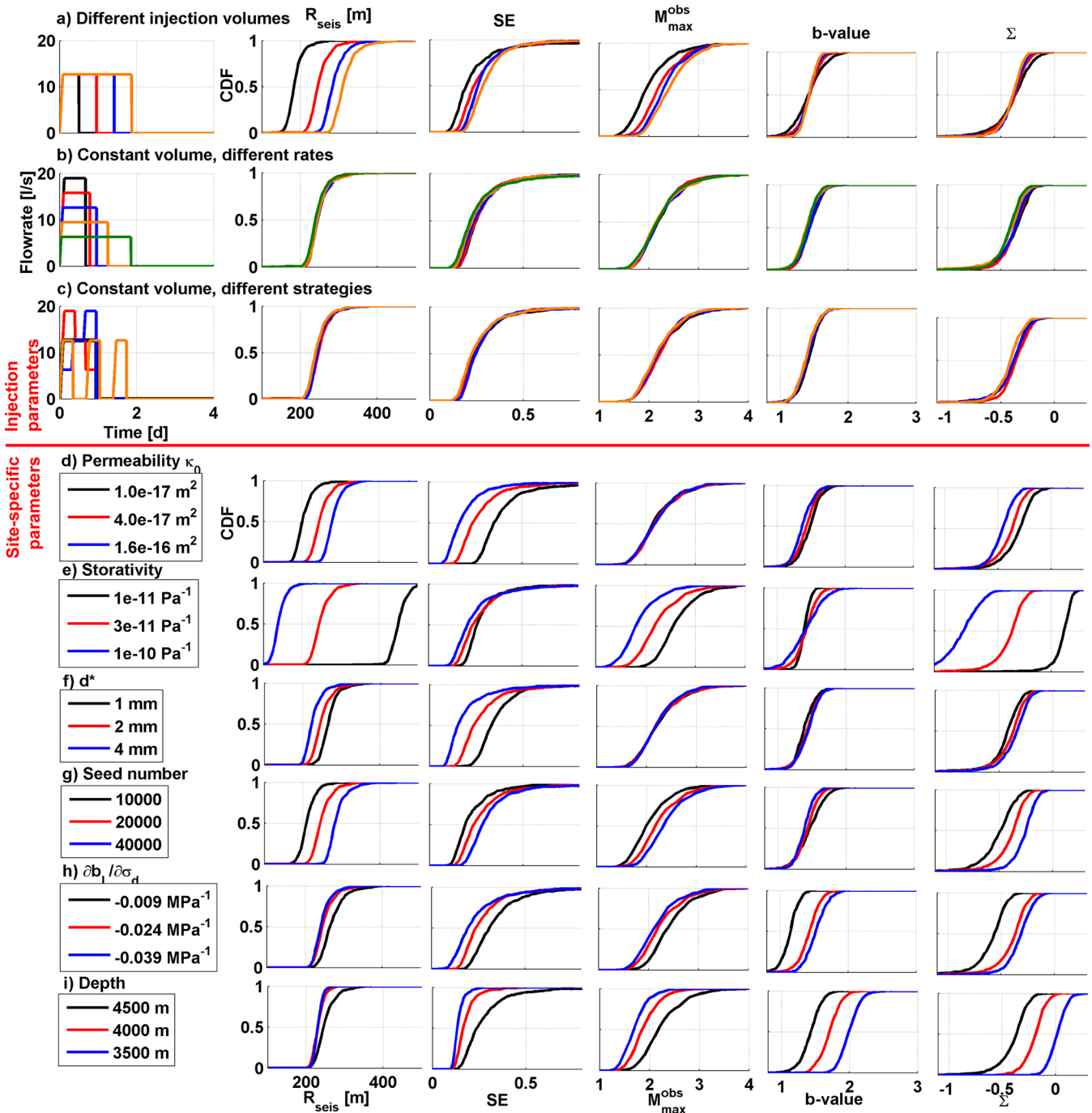
Figure 5. (a)–(c) Sensitivity of reservoir size, stimulation efficiency, maximum observed magnitude, *b*-value and seismogenic index to the injection volume, rate and strategy. (d)–(i) Sensitivity of the same parameters to various site-specific parameters.

conclude that *b*-value and Σ are not entirely site-specific but are to a certain degree dependent on the injection pressure. We stress, however, that the variability of those values (SE, *b*-value and Σ) for the same injection pressure outweighs the actual effect of injection rate on the median by far.

Third, we explore the role of the injection scheme by injecting at step-wise increasing or decreasing rates, or using three short pulses of constant rate each (Fig. 5c). The four different injection strategies explored here have hardly any impact on model results. Small changes are observed for SE, *b*-value and Σ, but these cannot be considered significant.

Note, however, that in the cases in Figs 5(b) and (c), we changed injection rate over a relatively small range. Lowering injection rate by orders of magnitude would certainly have a greater effect on seismicity. In the extreme case of injecting at almost zero pressure over long time periods would result in no seismicity in our models. Other effects (e.g. thermo-elastic effects, chemical alteration along fractures, etc.) may become a relevant mechanism for inducing seismicity in such situations. However, such cases are beyond the scope of this study, because we are interested in cases of short-term stimulation and induced seismicity (i.e. hours to days), where usually pressures on the order of >1–10 MPa are used.

In Figs 4(d)–(i), we explore the impact of site-specific parameters on the model results. Permeability, storativity and the coupling parameter d^* describe hydraulic properties of the reservoir rock. The number of seed points, which relates to the density of pre-existing fractures, the slope $\partial b_L/\partial \sigma_d$ in Fig. 1(c), and reservoir depth are parameters that determine the seismicity characteristics, while depth is also a design parameter that can be decided upon by the operators. R_{seis} depends on both hydraulic and seismicity-related parameters. The strongest change is observed for the hydraulic parameters, in particular for storativity. Similarly, SE is affected by most parameters. Note that all parameters except permeability have the same impact on both R_{seis} and SE; larger reservoir radii are related to higher stimulation efficiencies. In contrast, higher permeability instead leads to larger reservoirs, but to smaller stimulation efficiency, because reservoir pressure is lower and induces fewer events. $M_{max(obs)}$ strongly depends on storativity and depth. Storativity affects $M_{max(obs)}$ due to a purely geometric effect as has also been suggested by Shapiro *et al.* (2010) and Shapiro *et al.* (2013). Under low storativity conditions, a larger area is pressurized. Thus, more events are induced (hence also higher Σ), and the probability for a larger event magnitude also increases. Consequently, $M_{max(obs)}$ does not simply scale with the injected volume but rather with the size of the stimulated area. The stimulated rock volume and injection volume are connected via storativity. Depth impacts $M_{max(obs)}$ through the assumption that larger differential stress leads to lower b-values (Fig. 1c). Differential stress is lower at shallower depth, and thus the b-value is higher (Spada *et al.* 2013). Interestingly, permeability has no impact on $M_{max(obs)}$. Lower permeability leads to smaller pressurized areas for a given storativity, but pressure reaches higher levels. These two opposite effects cancel each other. The final b-value is most strongly influenced by $\partial b_L/\partial \sigma_d$ and reservoir depth. Σ is influenced by all parameters to some degree, whereas storativity and depth have the strongest impact. Note that for all seismicity-relevant parameters (i.e. number of seed points,

depth and $\partial b/\partial \sigma_d$), either reservoir size or stimulation efficiency or both are strongly related to $M_{max(obs)}$. We conclude from this sensitivity study that limiting $M_{max(obs)}$ can only be achieved by limiting reservoir size or stimulation efficiency (or both). Only by changing permeability, d^* and to some degree storativity—that is properties related to rock type—can larger reservoir sizes be achieved without trading it for a higher $M_{max(obs)}$.

Although stress drop and shear modulus have a potentially large effect on stimulation efficiency at a given amount of seismicity (Fig. 2), we decided do not systematically explore this sensitivity here. The reasons is that in our model magnitudes are first assigned (via a stochastic process), and then slip and source radius are computed from a given stress drop and shear modulus (eqs 3 and 5). Hence, increasing stress drop or shear modulus would result in lower stimulation efficiency. However, in reality a certain slip within a certain source radius occurs driven by fluid pressure, and larger stress drop and shear modulus would then result in larger magnitudes (i.e. magnitudes are not pre-assigned). Nevertheless, we can readily conclude from eqs (3) and (5) that higher stress drop and shear modulus would lead to higher induced seismic hazard for a certain reservoir size and stimulation efficiency.

3.3 Stimulation efficiency of larger magnitudes

The experiments in Figs 5(f), (h) and (i) are further investigated regarding the importance of different magnitude levels on stimulation efficiency. On the horizontal axis of Fig. 6, we show the magnitude threshold $M_{0.5SE}$, which signifies the magnitude above and below which 50 per cent of the total stimulation is produced. On the vertical axis, we show the number of events $N(M \geq M_{0.5SE})$ with magnitude larger than $M_{0.5SE}$ normalized to the total number of events N_{total} of each realization. The shape of the scatter in all experiments in Fig. 6 shows that the higher $M_{0.5SE}$ is, the fewer large events are involved in
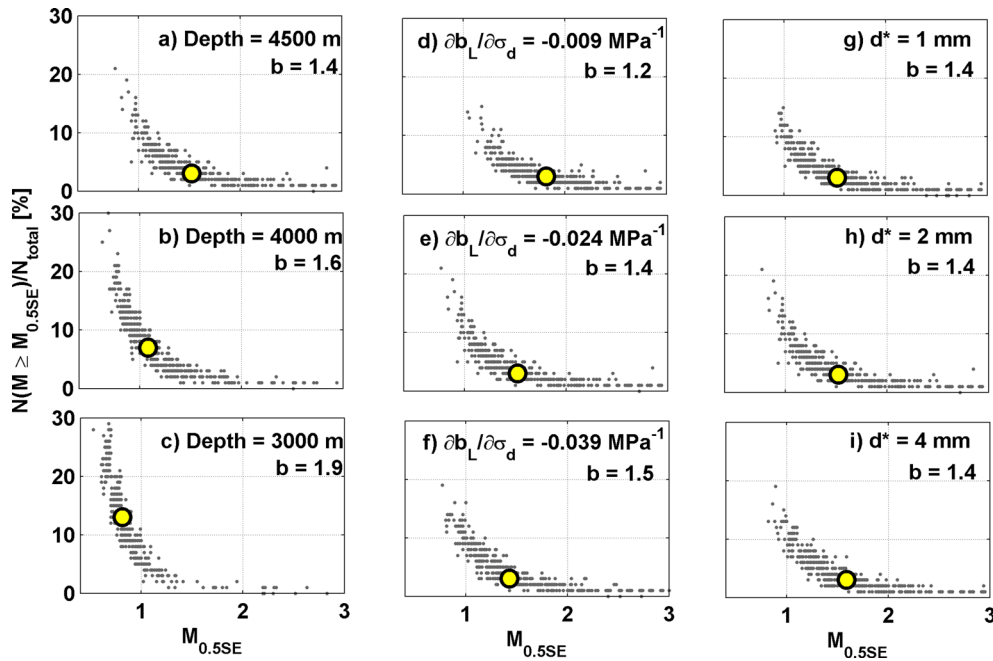

Figure 6. The magnitude threshold $M_{0.5SE}$ above and below which 50 per cent of the final stimulation efficiency is contributed plotted against the number of events with magnitude $M \geq M_{0.5SE}$ (normalized to the total number of events per realizations). Also shown is the median of both values (yellow circle). (a)–(c) Experiments varying depth corresponding to the ones in Fig. 5(i). (d)–(f) Experiments varying the gradient $\partial b_L/\partial \sigma_d$ as in Fig. 5(h). (g)–(i) Experiments varying the gradient $\partial b_L/\partial \sigma_d$ as in Fig. 5(f).

producing half of the stimulation. For the reference example shown in Fig. 4 (here in Fig. 6a) the median of $M_{0.5SE} = 1.5$, and the number of event magnitudes above that value are only about 3 per cent of the total number of events. $M_{0.5SE}$ depends on the final b-value (Figs 6a–f). For b-values of 1.2 and 1.9 the medians of $M_{0.5SE}$ become 1.8 and 0.8, and the number of event magnitudes above those values are 3 and 13 per cent, respectively. Thus, at high b-values of 1.9, all events between $M_c = 0.4$ and 0.8 contribute as much as the 13 per cent of all events with magnitudes larger than 0.8. The median values are not sensitive to d^* (Figs 6g–i). Even if d^* is small (i.e. permeability becomes maximally enhanced with very little slip) the stimulation efficiency of a few large event (here with $M > 1.5$) is as large as that of the smaller ones. We conclude that even if d^* tends towards 0 (i.e. instantaneous maximal permeability increase at onset of slip) would small events contribute little to stimulation because their source areas remain very small (eq. 3). We acknowledge, however, that the result also depends on (1) the choice on $\Delta\tau$ and G (Fig. 2) and (2) on the model for permeability growth chosen here (eq. 6). For the case of $\Delta\tau = 5.0$ MPa and $G = 10$ GPa shown in Fig. 2(d), 95 per cent of maximum stimulation is already reached even for events with $M \geq 0.7$. Note, however, that in this case the source radius decreases compared to the cases with lower $\Delta\tau$. Thus,

the stimulation efficiency of small events does not necessarily become much greater relative to large events. Finally, we also acknowledge that those results also depend on the magnitude of completeness here set to $M_c = 0.4$. Although for lower M_c the values of $M_{0.5SE}$ would decrease, the relative importance of a few large events in contrast to a large number of small events would remain.

3.4 Synthetic injection experiments

We further explore the implications of the sensitivity analysis in Section 3.2 for an injection scenario, in which seismic hazard is limited by regulatory obligations, as is the case in real injection operations. In Fig. 7, we present the results of a synthetic injection experiment, in which a constant flow rate of 12.5 l s^{-1} is injected and injection duration is controlled based on a traffic light system. Unlike the traffic light system suggested by Bommer *et al.* (2006), we here suggest an alternative based on probabilistic stop criteria for seismic hazard. Three stop criteria control the time of shut-in, i.e. injection is stopped (1) if the reservoir radius R_{seis} has reached the target reservoir size R_{stop}, (2) if the probability of exceeding a threshold magnitude M_t has exceeded 5 per cent based on the observed seismicity so far or (3) if the threshold magnitude M_t
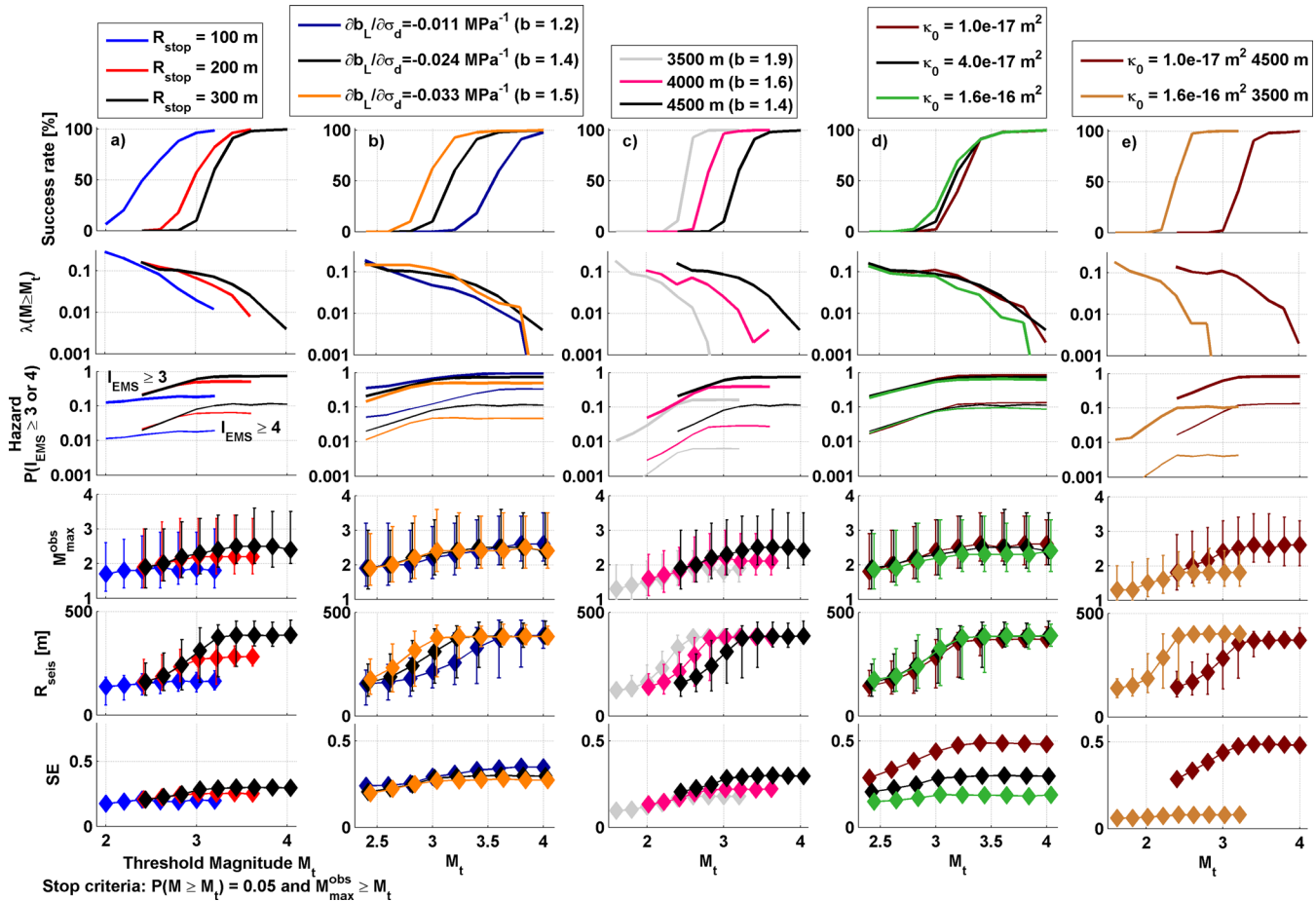
Figure 7. Injection experiment controlled by a probabilistic traffic light system. Injection is stopped, if (1) R_{stop} is reached, if (2) probability of exceeding M_t is more than 5 per cent, or if (3) M_t is exceeded. For each experiment we show the success rate, that is the number of time that the target reservoir radius R_{stop} is reached in 500 realizations; the rate $\lambda(M \geq M_t)$ of exceeding the threshold magnitude M_t; the probability of exceeding EMS intensity III (thick lines) and IV (thin lines); the maximum observed magnitude (including 95 per cent confidence intervals CI); the final reservoir radius (incl. 95 per cent CI); as well as the stimulation efficiency. (a) Experiments for different R_{stop}, and parameters in Table 1. (b) For different gradients $\partial b_L/\partial\sigma_d$ (all other parameters are the ones in Table 1; R_{stop} is 300 m). (c) For 4500, 4000 and 3500 m and depth, and thus different b-values. (c) For different initial permeability. (d) For a low hazard and a high hazard scenario.

has been exceeded. After stopping injection, the model is run for three more days to capture the majority of the post-shut-in effect. For each 500 realizations, we compute the success rate defined as the number of times that the target reservoir radius was reached (i.e. stop criterion 1), without having to stop due to seismic hazard (stop criteria 2 or 3). We also compute the rate $\lambda(M \geq M_t)$ at which the threshold magnitude M_t is exceeded in spite of the traffic light system (second row in Fig. 7). M_t may be exceeded due to post-shut-in seismicity, but also simply due to the fact that larger events can occur anytime in our model. Further, we also compute the hazard, expressed as the probability of exceeding the EMS Intensity $I_{EMS} = $ III or IV (European Macroseismic Scale; Gruenthal 1998) for each injection experiment. $P(I_{EMS} \geq$ III) corresponds to the probability of a felt event (third row in Fig. 7). We use the attenuation relationship by Faeh *et al.* (2011) to relate magnitude to intensity. M_{max}, R_{seis} and SE for each experiment are also shown in Fig. 7 (fourth, fifth and sixth row, respectively).

In Fig. 7(a), we use stop radii R_{stop} of 100, 200 and 300 m. The success rate increases for higher allowable hazard (i.e. higher M_t), and increases faster for small target reservoir sizes. We stress that a zero success rate does not imply full failure of the experiment, but only that the reservoir radius is smaller than planned. Note that at 100 per cent success rate the final reservoir radius is larger than the target reservoir size ($R_{seis} = 400$ m in case of $R_{stop} = 300$ m) due to the post-shut-in effect (i.e. a trailing effect caused by pressure diffusion continues to progress within the formation after shut-in). The results again demonstrate that reservoir size and seismic hazard are strongly connected. Larger reservoir sizes are achieved only at the expense of higher seismic hazard. The result is similar to the volumetric effect suggested by McGarr (1976). However, there is a major difference due to the probabilistic nature of our results. We do not estimate a single maximum expected magnitude $M_{max(exp)}$ from injection volume or reservoir size. Instead, the $M_{max(obs)}$ is strongly scattered, and the variability exceeds the change in the expected value with radius and allowable hazard (see fourth row in Fig. 7). Furthermore, despite controlling seismic hazard with a traffic light system, there still remains a chance, which may be called 'residual hazard or risk' that the predefined threshold hazard level is exceeded. For low M_t, the exceeding rate is larger than 10 per cent, although the threshold probability of exceeding it was set to 5 per cent only. Similarly, there still remains a more than 10 per cent chance for a felt event. On the one hand, this arises from the stochastic nature of the seismicity model that allows any magnitude to occur anytime, even if the overall frequency–magnitude distribution point to low hazard (i.e. when stop criterion 3 is met). On the other hand, this is a result of post-shut-in seismicity. Pressure diffusion does not cease immediately, and thus events larger than M_t may still occur after shut-in.

The effect of $\partial b_L/\partial \sigma_d$ is shown in Fig. 7(b). Steeper gradients of $\partial b_L/\partial \sigma_d$ produce higher total b-values. The probability for a felt event scales with the total b-value as expected: the lower the b-value, the higher the probability for a large event. Note, however, that the exceeding rate $\lambda(M \geq M_t)$ does not differ much, especially for low M_t (i.e. low success rates). Steeper gradients of $\partial b_L/\partial \sigma_d$ do not only produce higher total b-values, but also results in wider scattering and more extreme values for b_L (Fig. 1). Thus, even if the final b-value is higher, individual seed points are likely to have a b_L as low as 1.0, and magnitudes larger than M_t remain equally possible.

Fig. 7(c) shows results for different depths, which basically affects the b-value via the relationship $\partial b_L/\partial \sigma_d$. The b-values are 1.4, 1.6 and 1.9 for depths of 4500, 4000 and 3500 m, respectively. For cases

with larger b-values, the success rate improves at lower M_t. The rate of exceeding M_t and the probability for a felt event are also smaller for high b-values, and also M_{max} becomes smaller. Unlike the case in Fig. 7(b), the overall level of b_L at seed points is higher, but the scattering of b_L remains about the same for different depths (Fig. 1). Thus, the rate of magnitudes greater than M_L strongly decreases for shallower depth. Note, however, that higher b-values also result in lower stimulation efficiency.

Fig. 7(d) shows that injection in a more permeable rock mass has little impact on the success rate. However, higher permeability results in lower rates of exceeding M_t, a lower probability for a felt event and lower $M_{max(obs)}$. The trade-off is that stimulation efficiency is strongly degraded for higher permeability.

Since high b-values and high permeability have an advantageous impact on hazard and success rate, we compare two opposite scenarios in Fig. 7(e): (1) low permeability at 4500 m depth (mean b-value = 1.4) and (2) high permeability at 3500 m depth (mean b-value = 1.9). Success rate becomes high and hazard low for the scenario at shallower depth and higher permeability. Also the maximum observed magnitude is lower. However, stimulation efficiency drops to 0.08, while for the high hazard scenario the stimulation efficiency is 0.48. Using eq. (13), we can derive that the effective stimulation factor is $S_{eff} = 17$ and 96, for the low and high hazard scenarios, respectively. Thus, in the low hazard case an average permeability $k_{eff} = S_{eff} \cdot k_0 = 2.7\text{e--}15$ m^2 was reached, which is a factor 2.8 times larger than the one reached in the high hazard case ($k_{eff} = 9.6\text{e--}16$ m^2). We conclude—in a qualitative manner— that rock masses with higher initial permeability and a tendency to higher b-values may yield a much lower induced seismic hazard, whereas the target reservoir size and properties can still be achieved.

An alternative possibility to achieve higher stimulation efficiency under high b-value conditions would be to stimulate a series of fractures next to each other. To illustrate this, we take the case in Fig. 7(c) at 3500 m depth which has a b-value of 1.9 and $M_t = 2.6$ ($k_0 = 4\text{e-}17$ m^2) as example in a scoping calculation. The success rate for that experiment is 93 per cent and the stimulation efficiency is SE = 0.18, which corresponds to $S_{eff} = 37$ and $k_{eff} = 1.5\text{e--}15$ m^2. Note that this value corresponds to the equivalent porous medium permeability of a single fracture in a 100 m open-hole section. If this section would contain 10 such fractures at an average spacing of 10 m, the equivalent porous medium permeability would be $10 k_{eff} = 1.5\text{e--}14$ m^2. However, also the rate of exceeding M_t increase from 0.012 to 0.12, and the probability for a felt event increases from 16 per cent to about 82 per cent.

In a real stimulation there may be not only a target reservoir size, but also a target permeability that is required to create a productive reservoir. In our numerical experiment, we can define a target stimulation factor that has to be achieved by stimulating several fractures. Such an experiment is done in Fig. 8 based on the simulations in Fig. 7(c). We aim for an equivalent porous medium permeability that is enhanced by a factor 200 along the open-hole section of 100 m. Thus, for the experiments in Fig. 7(c), we compute the effective stimulation factor S_{eff} for each realization. The average values are shown in Fig. 8(b). The maximum value for $b = 1.4$ is about 60, and for $b = 1.9$ about 37. Based on those values, we compute the number of fractures N_f with average stimulation factor S_{eff} that have to be stimulated to reach an total effective stimulation factor of $S_{eff}(N_f) = 200$ (Fig. 8c). For experiments with 100 per cent success rate, only three to four fractures are required in the case of $b = 1.4$, while for $b = 1.9$ five to six fractures are required. Note that although both the exceeding rate (Fig. 8d), and seismic hazard (Fig. 8e) scale with the number of required fractures, the exceeding
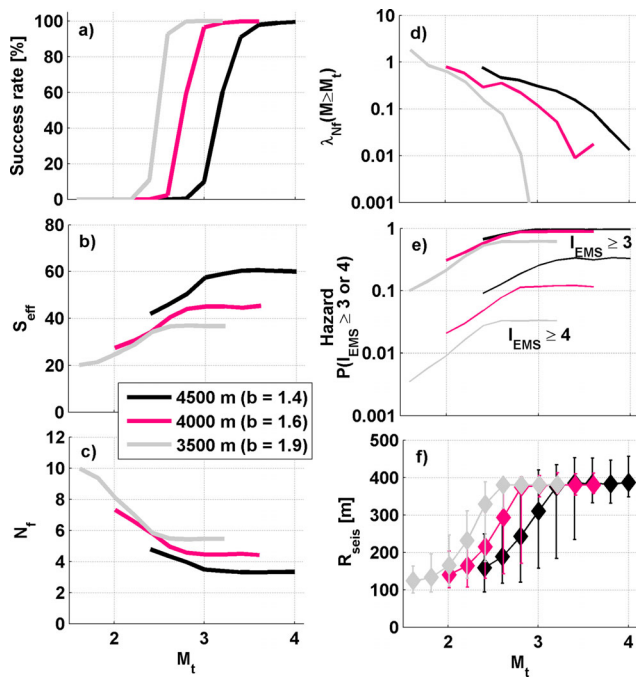
Figure 8. (a) Success rate of experiments shown in Fig. 7(c). (b) Effective stimulation factor S_{eff}. (c) Number of fractures N_f required to reach a total effective stimulation factor $S_{eff}(N_f) = 200$ over a 100 m open hole section. (d) Rate of exceeding M_t during stimulation of N_f fractures. (e) Probability of exceeding EMS intensities 3 and 4 during N_f stimulations. (f) Final reservoir radius R_{seis} per fracture.

rate and hazard is still the lowest for the highest *b*-value. Thus, in injection experiments with high *b*-values the same permeability enhancement can be achieved as in those with low *b*-value by stimulating multiple fractures, and, at the same time, with still lower costs of seismic hazard (Figs 8d and e). In addition, the success rate in high *b*-value stimulations is higher. Not only can a certain target permeability be created with lower seismic hazard, but also the chance to reach a larger reservoir radius is better. For instance, at a threshold magnitude $M_t = 2.6$, the stimulated fractures have an end radius of 190, 300 and 380 m for $b = 1.4$, 1.6 and 1.9, respectively. At the same time, $M_t = 2.6$ is exceeded with rates of 0.47, 0.27 and 0.08, respectively.

4 DISCUSSION AND CONCLUSIONS

The main conclusions of this study are summarized as follows:

(1) Larger magnitude events stimulate reservoirs more efficiently. In the reference model in Fig. 4, the 3 per cent of all events that are larger than $M1.5$ contribute as much to stimulation as the remaining 97 per cent with magnitudes $0.4 \leq M \leq 1.5$. In the case shown in Fig. 3, six events with $M \geq 1.6$ contribute as much to permeability enhancement as the other 158 events. The contribution of large events becomes somewhat less important, if the *b*-value increases (Fig. 6). Nevertheless, small events are less efficient in stimulating, because they are not only associated with less slip, but also because slip occurs on smaller sources areas. Although larger events (e.g. $M \geq 1.5$) occur far less frequent, they are much more important for effective stimulation compared to the many smaller events.

(2) Due to the intrinsic randomness and unpredictability that is characteristic for induced seismicity, planning of target reservoir properties along with the expected induced seismic hazard is diffi-

cult (Fig. 4). In a real injection experiment, the unpredictable reservoir response is additionally affected by the limited knowledge of the site conditions. Thus, real-time monitoring of seismicity, reservoir size, and permeability in connection with a hazard-based traffic light system is essential.

(3) Site-specific parameters potentially have a larger impact on induced seismic hazard and reservoir properties, than changing injection strategy (Fig. 5). Only injection volume has an impact that can emerge above the variability of the results.

(4) Induced seismic hazard is strongly connected to the target reservoir properties (namely reservoir size and degree of stimulation), and the site specific conditions. At a given site, a productive reservoir can only be achieved at the cost of a certain seismic hazard and risk.

(5) High *b*-values and high initial permeability are favourable for reaching a target reservoir size while keeping the seismic hazard low. Lower seismic hazard may imply that the reservoir is not stimulated well, but if initial permeability is already high the reservoir may still become productive even at lower stimulation efficiency. Alternatively, a required degree of permeability enhancement can be reached by stimulating several fractures. Provided that the *b*-value is high, the expense in seismic hazard may not necessarily become inacceptable.

We acknowledge that the model approach here is limited due to several assumptions. Three of the most critical assumptions are highlighted here:

(1) We limit our modelling to 2-D, which implies that all flow, slip and permeability enhancement occurs in one single fracture or fracture zone. A more realistic model would have to include a 3-D fracture network in which hydraulic properties are altered through hydroshearing in a much more complex manner. In addition, fracture connectivity becomes a relevant issue. We argue, however, that the aforementioned conclusions still remain valid from a qualitative point of view. In particular, also the relative importance of small events in enhancing permeability may decrease even stronger, as slip of smaller events does not accumulate, if they do not occur on the same fracture patch. Smaller events would also contribute less to fracture connectivity.

(2) The relationship between event magnitude and permeability increase is strongly dependent on scaling laws that relate magnitude to slip and source area. They treat potentially complex earthquake sources as circular shaped and with constant slip and stress drop. Also, the relationship between slip and permeability change is poorly constraint, and based only on the laboratory observations of Esaki *et al.* (1999) and Lee & Cho (2002), and on an ad-hoc parameterization. The limiting permeability enhancement S_L may be different, and the permeability may increase faster, slower, or even in a different manner. However, increasing S_L at constant d^* would lead to even more divergence between the importance of small and large events. Decreasing d^* would enhance the importance of small events somewhat. Because the lesser contribution of small events is not only a result of smaller slip, but also because slip occurs over a smaller source area, the stimulation efficiency of small earthquakes would remain minor compared to large earthquakes. Hence, we argue that the main conclusions of the study persist qualitatively despite possible deviation from our assumptions on scaling of source parameters and permeability change.

(3) The relationship between differential stress and local *b*-values is poorly constrained in literature. Observations of a possible relationship between stress and *b*-values are only qualitative in literature (Schorlemmer *et al.* 2005; Amitrano 2012; Spada *et al.* 2013). The

value used here for the reference model (Figs 3 and 4) is the one found by Gischig & Wiemer (2013) to best-fit induced seismicity observations in the Basel EGS project. However, the *b*-value change with depth is much exaggerated in comparison with the *b*-value depth dependence found by Spada *et al.* (2013) for tectonic events. Nevertheless, results related to effects of different *b*-values depend only on the final *b*-value and not on this relationship; similar conclusions may be obtained with b_L independent of stress.

The results presented here are considered conservative concerning seismic hazard (i.e. exaggerated hazard) for the following two reasons:

First, event magnitudes are here generated by a stochastic process and not based on an appropriate representation of the source physical processes. We allow any event magnitude to occur anytime as long as it satisfies the Gutenberg–Richter distribution. The approach corresponds to the conservative end member in the discussion on the maximum possible magnitude during injection. While in our model the frequency–magnitude distribution is not truncated at any large magnitude, other opinions in literature state that the maximum possible moment release corresponds to the one that is required to accommodate the injected volume (McGarr 1976; Baisch *et al.* (2009), and can be estimated from the stimulated rock mass volume. Thus, the maximum possible magnitude is limited, and the frequency-magnitude distribution can be truncated at relatively small events (e.g. $M_w = 3.7$ for Basel, Baisch *et al.* 2009). This other optimistic end member neglects the fact that a highly critically stressed fault may run out beyond the pressurized area with the aid of tectonic stress once it is triggered by injection. Models by Garagash & Germanovic (2012) demonstrate that such behaviour is possible. Nevertheless, while we agree that there may be an upper magnitude limit related to injection volume, there is currently no conclusive scientific basis to estimate it, to the best of our knowledge.

Second, in the presented model all slip and permeability enhancement occurs in connection with seismic events. However, it is well known (but rarely quantified) that aseismic slip may also occur during reservoir stimulation as inferred in Soultz-sous-forêt (Cornet *et al.* 1997; Evans *et al.* 2005) and from numerical models (Garagash & Germanovic 2012; Zoback *et al.* 2012). As our model neglects a potential aseismic component of slip and dilation, the results are conservative regarding the connection between permeability creation and seismic hazard.

Despite those limitations, the aforementioned conclusions are still valid and can be appreciated in a qualitative manner. Motivated by the results regarding optimal conditions for stimulation, it remains to be discussed where such favourable site conditions can be found. Initial permeability strongly depends on rock type, the degree of fracturing, and likely also on depth (i.e. permeability tends to increase at shallow depths; e.g. Ingebritsen & Manning 2010). Higher *b*-values may be found at shallower depth (Fig. 7; Spada *et al.* 2013) or at normal faulting regimes (Schorlemmer *et al.* 2005), or in volcanic areas (Wiemer & Wyss 2002). In particular, in volcanic areas (e.g. In New Zealand or Iceland) or regions with high geothermal gradients (The Geysers, California) several favourable conditions coincide. Due to high geothermal gradients shallow depths can be targeted, where natural permeability is expected to be high (Ingebritsen & Manning 2010). In addition, tectonic *b*-values are likely to be high due to shallow depth (Spada *et al.* 2013), and volcanic activity (Wiemer & Wyss 2002). However, structural properties of a fractured rock mass potentially have a strong impact on the *b*-value, too (King 1983). Such properties are reflected in ob-

servable stress heterogeneities. Day-Lewis *et al.* (2010) showed that the fractal properties of stress fluctuations are related to the *b*-value of tectonic earthquakes nearby. Similarly, fracture orientations and spacing may have an impact on *b*-values. Terakawa *et al.* (2012) pointed out for the EGS project in Basel that the largest magnitudes may all have occurred on faults with large shear stress and that were triggered with little overpressure. Many small events, instead, occurred on faults that were not optimally oriented in the stress field. Thus, there may be a relationship between *b*-value and orientation of pre-existing fractures that are stimulated. Similarly, Zoback *et al.* (2012) point out, that pre-existing fractures that are not optimally oriented in the stress field may have a larger tendency for aseismic slip. Recognizing fractures and rock types that favour aseismic slip would be advantageous to reducing seismicity during stimulation, without necessarily reducing stimulation efficiency. Unfortunately, laboratory experiments, site observations and numerical studies are currently not comprehensive enough for pointing to optimal rock mass conditions.

Our study only provides conceptual results on the relationship between seismicity and reservoir properties, and is backed up by observations only to some degree. However, they are targeted to motivate more systematic research between site-specific conditions, geology and induced seismicity. The above results can serve as hypotheses to be tested in numerical modelling experiments, in laboratory tests, or in *in situ* tests in future EGS project or dedicated underground rock laboratories.

REFERENCES

Amitrano, D., 2012. Variability in the power-law distributions of rupture events, *Eur. Phys. J. Spec. Top.,* **205,** 199–215.

Bachmann, C.E., Wiemer, S., Goertz-Allmann, B.P. & Woessner, J., 2012. Inuence of pore-pressure on the event-size distribution of induced earthquakes, *Geophys. Res. Lett.,* **39,** L09302, doi:10.1029/2012GL051480.

Baisch, S. *et al.*, 2009. Deep heat mining Basel: seismic risk analysis, Technical report SERIANEX, edited.

Bommer, J.J., Oates, S., Cepeda, J.M., Lindholm, C., Bird, J., Torres, R., Marroquín, G. & Rivas, J., 2006. Control of hazard due to seismicity induced by a hot fractured rock geothermal project, *Eng. Geol.,* **83,** 287–306.

Cappa, F., Rutqvist, J. & Yamamoto, K., 2009. Modeling crustal deformation and rupture processes related to upwelling of deep CO_2-rich fluids during the 1965–1967 Matsushiro earthquake swarm in Japan, *J. geophys. Res.,* **115,** B10304, doi:10.1029/2009JB006398.

Cladouhos, T.T., Petty, S. & Nordin, Y., 2013. Microseismic monitoring of Newberry volcano EGS demonstration, in *Proceedings of 38th Workshop on Geothermal Reservoir Engineering,* Stanford University, Stanford, California, February 11–13, SGP-TR-198.

Cornet, F.H., Helm, J., Poitrenaud, H. & Etchecopar, A., 1997. Seismic and aseismic slip induced by large fluid injections, *Pure appl. Geophys.,* **150,** 563–583.

Day-Lewis, A., Zoback, M. & Hickman, S., 2010. Scale-invariant stress orientations and seismicity rates near the San Andreas fault, *Geophys. Res. Lett.,* **37,** L24304, doi:10.1029/2010GL045025.

de Pater, C.J. & Baisch, S., 2011. Geomechanical study of Bowland Shale seismicity: Cuadrilla Resources Ltd., Synthesis Report, Available at: wi-jzijn.europamorgen.nl (last accessed November 2011).

Ellsworth, W.L., 2013. Injection-induced earthquakes, *Science,* **341,** doi:10.1126/science.1225942.

Esaki, T., Du, S., Mitani, Y., Ikusada, K. & Jing, L., 1999. Development of a shear-flow test apparatus and determination of coupled properties for a single rock joint, *Int. J. Rock Mech. Min. Sci.,* **36,** 641–650.

Eshelby, J.D., 1957. The determination of the elastic field of an ellipsoidal inclusion and related problems, *Proc. R. Soc. Lond.,* **241,** 376–396.

Evans, K.F., 2005. Permeability creation and damage due to massive fluid injections into granite at 3.5 km at Soultz: 2. Critical stress and fracture strength, *J. geophys. Res.,* **110,** B04204, doi:10.1029/2004JB003169.

Evans, K.F. *et al.*, 2005. Microseismicity and permeability enhancement of hydrogeologic structures during massive fluid injections into granite at 3 km depth at the Soultz HDR site, *Geophys. J. Int.,* **160,** 388–412.

Evans, K.F., Zappone, A., Kraft, T., Deichmann, N. & Moia, F., 2012. A survey of the induced seismic responses to fluid injection in geothermal and CO_2 reservoirs in Europe, *Geothermics,* **41,** 30–54.

Faeh, D. *et al.*, 2011. ECOS-09 earthquake catalogue of Switzerland release 2011, Report and Database, Public Catalogue, Report SED/RISK, edited, Swiss Seismological Service ETH, Zürich.

Garagash, D.I. & Germanovich, L.N., 2012. Nucleation and arrest of dynamic slip on a pressurized fault, *J. geophys. Res.,* **117,** B10310, doi:10.1029/2012JB009209.

Giardini, D., 2009. Geothermal quake risks must be faced, *Nature,* **461,** 848–849.

Gischig, V.S. & Wiemer, S., 2013. A stochastic model for induced seismicity based on non-linear pressure diffusion and irreversible permeability enhancement, *Geophys. J. Int.,* **194**(2), 1229–1249.

Goertz-Allmann, B.P. & Wiemer, S., 2013. Geomechanical modeling of induced seismicity source parameters and implications for seismic hazard assessment, *Geophysics,* **78**(1), KS25–KS39.

Goertz-Allmann, B.P., Goertz, A. & Wiemer, S., 2011. Stress drop variations of induced earthquakes at the Basel geothermal site, *Geophys. Res. Lett.,* **38**(9), L09308, doi:10.1029/2011GL047498.

Gruenthal, G., ed., 1998. *European Macroseismic Scale 1998 (EMS-98),* Cahiers du Centre Europeen de Geodynamique et de Seismologie 15.

Hanks, T. & Kanamori, H., 1979. A moment magnitude scale, *J. geophys. Res.,* **84,** 2348–2350.

Häring, M.O., Schanz, U., Ladner, F. & Dyer, B.C., 2008. Characterisation of the Basel 1 enhanced geothermal system, *Geothermics,* **37,** 469–495.

Ingebritsen, S.E. & Manning, C.E., 2010. Permeability of the continental crust: dynamic variations inferred from seismicity and metamorphism, *Geofluids,* **10,** 193–205.

Kaieda, H., Jones, R., Moriya, H., Sasaki, S. & Ushijima, K., 2005. Ogachi HDR reservoir evaluation by AE and geophysical methods, in *Proceedings of World Geothermal Congress 2005,* Antalya, Turkey, April 24–29.

Keranen, K.M., Savage, H.M., Abers, G.A. & Cochran, E.S., 2013. Potentially induced earthquakes in Oklahoma, USA: links between wastewater injection and the 2011 M_w 5.7 earthquake sequence, *Geology,* **41**(6), 699–702.

King, G.C.P., 1983. The accommodation of large strains in the upper lithosphere of the Earth and other solids by self-similar fault systems: the geometrical origin of b-value, *Pure appl. Geophys.,* **121,** 761–815.

Lee, H.S. & Cho, T.F., 2002. Hydraulic characteristics of rough fractures in linear flow under normal and shear load, *Rock Mech. Rock Eng.,* **35**(4), 299–318.

Majer, E.L., Baria, R., Stark, M., Oates, S., Bommer, J., Smith, B. & Asanuma, H., 2007. Induced seismicity associated with Enhanced Geothermal Systems, *Geothermics,* **36**(3), 185–222.

Majer, E., Nelson, J., Robertson-Tait, A., Savy, J. & Wong, I., 2012. Protocol for addressing induced seismicity associated with enhanced geothermal systems, U.S. Department of Energy, Energy Efficiency and Renewable Energy.

McClure, M. & Horne, R., 2011. Investigation of injection-induced seismicity using a coupled fluid flow and rate/state friction model, *Geophysics,* **76**(6), 181–198.

McGarr, A., 1976. Seismic moments and volume changes, *J. geophys. Res.,* **81**(8), 1487–1494.

Miller, S.A., Collettini, C., Chiaraluce, L., Cocco, M., Barchi, M. & Kaus, B.J.P., 2004. Aftershock driven by a high pressure CO_2 source at depth, *Nature,* **427,** 724–727.

Mitchell, T.M. & Faulkner, D.R., 2008. Experimental measurements of permeability evolution during triaxial compression of initially intact crystalline rocks and implications for fluid flow in fault zones, *J. geophys. Res.,* **113,** B11412, doi:10.1029/2008JB005588.

Petty, S., Nordin, Y., Glassely, W. & Cladouhos, T., 2013. Improving geothermal project economics with multi-zone stimulation: results from the Newberry volcano EGS demonstration, in *Proceedings of 38th Workshop on Geothermal Reservoir Engineering,* Stanford University, Stanford, California, February 11–13, SGP-TR-198.

Rothert, E. & Shapiro, S.A., 2003. Microseismic monitoring of borehole fluid injections: data modeling and inversion for hydraulic properties of rocks, *Geophysics,* **68,** 685–689.

Schorlemmer, D., Wiemer, S. & Wyss, M., 2005. Variations in earthquakesize distribution across different stress regimes, *Nature,* **437,** 539–542.

Shapiro, S.A., Dinske, C., Lagenbruch, C. & Wenzel, F., 2010. Seismogenic index and magnitude probability of earthquakes induced during reservoir fluid stimulations, *Leading Edge,* **29,** 304–309.

Shapiro, S.A., Krüger, O.S. & Dinske, C., 2013. Probability of inducing given-magnitude earthquakes by perturbing finite volumes of rocks, *J. geophys. Res.-Solid Earth,* **118,** 3557–3575.

Spada, M., Tormann, T., Goebel, T. & Wiemer, S., 2013. Generic dependence of the frequency-size distribution of earthquakes on depth and its relation to the strength profile of the crust, *Geophys. Res. Lett.,* **40**(4), 709–714.

Terakawa, T., Miller, S.A. & Deichmann, N., 2012. High fluid pressure and triggered earthquakes in the enhanced geothermal system in Basel, Switzerland, *J. geophys. Res.,* **117,** B07305, doi:10.1029/2011JB008980.

Voss, C.I. & Provost, A.M., 2010. SUTRA—a model for saturated-unsaturated, variable-density ground-water flow with solute or energy transport, U.S. Geological Survey Water-Resources Investigations report 02–4231, 300 p. Available at: http://water.usgs.gov/nrp/gwsoftware (last accessed 22 September 2010).

Wiemer, S. & Wyss, M., 2002. Mapping spatial variability of the frequency-magnitude distribution of earthquakes, *Adv. Geophys.,* **45,** 259–302.

Zoback, M., Kohli, A., Das, I. & McClure, M., 2012. The importance of slow slip on faults during hydraulic fracturing stimulation of shale gas reservoirs, SPE 155476, in *Paper presented at the SPE Americas Unconventional Resources Conference,* Pittsburgh, PA, USA, doi:10.2118/155476-MS.